eChem
https://www.sciltp.com/journals/eChem



Article

Interlayer Engineering by Ionic-Liquid Cation Pre-Intercalation for High-Performance Aqueous Zinc-Ion Batteries

Yuqing Ji †, Helixin Jiao †, Keyi Chen, Zhuojin Li, Da Chen, Qiaoling Kang and Quan Zong *

College of Materials and Chemistry, China Jiliang University, Hangzhou 310018, China
* Correspondence: quanzong@cjlu.edu.cn
† These authors contributed equally to this work.

How To Cite: Ji, Y.; Jiao, H.; Chen, K.; et al. Interlayer Engineering by Ionic-Liquid Cation Pre-Intercalation for High-Performance Aqueous Zinc-Ion Batteries. *eChem* **2026**, *2*(2), 13. https://doi.org/10.53941/echem.2026.100013

Received: 14 September 2026
Revised: 20 October 2026
Accepted: 5 November 2026
Published: 13 November 2026

Abstract: Layered vanadium oxides are promising cathode materials for aqueous zinc ion batteries (ZIBs), yet their practical application is constrained by sluggish Zn^{2+} transport, structural instability, and continuous vanadium dissolution. Herein, we introduce an ionic-liquid cation pre-intercalation strategy to reconstruct the interlayer microenvironment of hydrated vanadium pentoxide (VOH) using 1-butyl-3-methylimidazolium ($BMIM^+$). The hydrophobic butyl chain shields the vanadium oxide framework from excessive water-mediated degradation while serving as a molecular pillar to expand the interlayer spacing, whereas the polar imidazolium moiety tailors the structural and electronic environment and provide additional favorable environments for Zn^{2+} storage. Beyond interlayer expansion, $BMIM^+$ pre-intercalation induces oxygen vacancies and enhances electronic conductivity, while theoretical calculations reveal a substantially reduced Zn^{2+} migration barrier. Benefiting from this synergistic interlayer regulation, the optimized cathode delivers 452 mAh g^{-1} at 0.1 A g^{-1} and 247 mAh g^{-1} at 10 A g^{-1}, while retaining 90.3% of its initial capacity after 8000 cycles at 8 A g^{-1}. This organic ionic-liquid pre-intercalation strategy simultaneously stabilizes the host framework and accelerates ion transport, providing a versatile route toward durable, high-rate layered cathodes for advanced ZIBs.

Keywords: vanadium oxides; interlayer engineering; ionic liquid cations; aqueous zinc ion batteries

1. Introduction

The rapid growth of renewable energy, particularly solar and wind power, is changing the global energy landscape. However, the intermittent nature of these energy sources leads to a mismatch between electricity generation and consumption. Therefore, there is an increasing need for large-scale energy-storage systems that are safe, low-cost, and reliable [1–4]. Lithium-ion batteries are widely used because of their mature technology and high energy density. However, their further application in large-scale energy storage is still limited by safety and resource concerns [5,6]. The use of flammable organic electrolytes can cause serious safety risks, particularly under high-temperature or abusive conditions. In addition, the limited availability and increasing cost of lithium resources may restrict their large-scale deployment in the future [7,8]. Aqueous zinc ion batteries (ZIBs) have attracted increasing attention as a promising alternative for large-scale energy storage. Their aqueous electrolytes are nonflammable, providing an important advantage in terms of safety [9,10]. Moreover, zinc is abundant, low-cost, and widely available, making ZIBs particularly attractive for sustainable and economical energy-storage

Copyright: © 2026 by the authors. This is an open access article under the terms and conditions of the Creative Commons Attribution (CC BY) license (https://creativecommons.org/licenses/by/4.0/).
Publisher's Note: Scilight stays neutral with regard to jurisdictional claims in published maps and institutional affiliations.

applications [11–13]. Nevertheless, further development of ZIBs requires electrode materials with high capacity, fast reaction kinetics, and long-term structural stability.

Hydrated vanadium oxides have been widely investigated as cathode materials for ZIBs because of their layered structure, high theoretical capacity, and flexible ion storage chemistry [14,15]. However, the practical performance of these materials is often limited by their narrow interlayer spacing and poor structural stability [16,17]. During repeated Zn^{2+} insertion/extraction, the strong electrostatic interaction between divalent Zn^{2+} and the vanadium oxide layers may lead to sluggish ion transport, lattice distortion, and even structural collapse [18,19]. In addition, the dissolution of vanadium species in aqueous electrolytes further accelerates capacity decay during long-term cycling [20,21]. Therefore, rational regulation of the interlayer structure and local chemical environment is essential for improving the electrochemical performance and cycling stability of hydrated vanadium oxide cathodes. Pre-intercalation has proven to be an effective approach for regulating the layered structure of vanadium oxides. A variety of guest species, including metal cations, inorganic ions, and organic molecules, have been introduced into the interlayer galleries to enlarge the interlayer spacing, stabilize the host framework, and improve Zn^{2+} diffusion kinetics [22–24]. Among them, organic cations are particularly attractive because their molecular structure can be readily adjusted, allowing simultaneous regulation of interlayer spacing and interlayer interactions [25,26]. Moreover, the incorporation of organic species can introduce new chemical interactions within the layered framework, providing an opportunity to tune the local environment for Zn^{2+} storage beyond simple structural expansion. Nevertheless, most reported intercalation strategies primarily rely on enlarging the interlayer distance, while the role of the chemical environment created by the intercalated species in regulating ion transport and structural stability remains insufficiently understood.

Herein, we report a 1-butyl-3-methylimidazolium cation ($BMIM^+$) pre-intercalated hydrated vanadium oxide (BVOH) as a stable and kinetically favorable cathode for aqueous ZIBs. The pre-intercalated $BMIM^+$ acts as a multifunctional interlayer regulator that reconstructs both the structural and chemical environments of the hydrated vanadium oxide. Its incorporation expands the interlayer spacing and weakens the interlayer interactions, thereby creating more accessible diffusion channels and promoting Zn^{2+} transport. Meanwhile, $BMIM^+$ incorporation induces oxygen vacancies and provides additional electrochemically active sites for Zn^{2+} storage. Notably, the hydrophobic butyl moieties of $BMIM^+$ partially regulate the interlayer water environment, reducing the amount of confined water and mitigating the water-induced structural degradation of the vanadium oxide framework. As a result, BVOH achieves high capacity (452 mAh g^{-1} at 0.1 A g^{-1}), enhanced charge storage kinetics (247 mAh g^{-1} at 10 A g^{-1}), and improved structural stability during cycling (90.3% of its initial capacity after 8000 cycles at 8 A g^{-1}).

2. Experimental Section

2.1. Synthesis of VOH and BVOH

All chemical reagents were used as received without further purification. Typically, 2 mmol of V_2O_5 (99.5%, Aladdin) was first dispersed in 80 mL of deionized water under vigorous magnetic stirring. Subsequently, 2 mL of 30 wt% H_2O_2 (30 wt.%, Aladdin) solution was slowly added dropwise, and the suspension was continuously stirred at room temperature for 30 min. Afterward, 0.5 mmol of 1-butyl-3-methylimidazolium chloride (98%, Aladdin) was added, followed by an additional 15 min of stirring to ensure homogeneous mixing. The resulting precursor solution, together with a piece of pretreated carbon cloth (1 cm × 1 cm, WOS1011, 0.35 mm-thickness, 1.5 mΩ cm^2, CeTech Co., Ltd., Taichung, Taiwan), was transferred into a 100 mL Teflon-lined stainless-steel autoclave and subjected to hydrothermal treatment at 120 °C for 6 h. Upon cooling, the carbon cloth-supported product was collected, thoroughly rinsed with deionized water and ethanol, and vacuum-dried at 60 °C for 12 h. As a control, VOH was synthesized following the same procedure, except that no imidazolium salt was introduced into the precursor solution. The mass loadings of VOH and BVOH are approximately 0.8 mg cm^{-2} and 1.3 mg cm^{-2}, respectively.

2.2. Materials Characterization

The crystal structure of the as-prepared samples was analyzed by X-ray diffraction (XRD, Rigaku (Tokyo, Japan) D/Ultima IV) employing Cu K_α radiation (λ = 1.5418 Å). Surface elemental compositions and corresponding chemical states were determined using X-ray photoelectron spectroscopy (XPS, Thermo Scientific (Waltham, MA, USA) K-Alpha). The vibrational characteristics of the samples were examined by Fourier-transform infrared spectroscopy (FTIR, Thermo Fisher Scientific (Waltham, MA, USA) Nicolet iS5) over 600–4000 cm^{-1}, while Raman spectra were acquired using a HORIBA LabRAM Odyssey Raman microscope with a 514 nm laser excitation. Thermogravimetric analysis coupled with differential scanning calorimetry (TG-DSC, Netzsch (Selb, Germany) STA 449 F3) was performed in flowing air from 30 to 600 °C at a heating rate of 10 °C min^{-1} to assess the thermal behavior and organic component content. The morphology and microstructural features were

investigated by field-emission scanning electron microscopy (FESEM, (JEOL, Tokyo, Japan) JSM-IT800) and transmission electron microscopy (TEM, (JEOL, Tokyo, Japan) JEM-2100F). Moreover, elemental spatial distributions were mapped by energy-dispersive X-ray spectroscopy (EDS) integrated with the TEM system.

2.3. Electrochemical Measurements

Electrochemical properties were assessed in CR2032-type coin cells assembled in ambient air. The carbon cloth loading the active material was directly used as the cathode, while Zn foil served as the anode. A glass-fiber membrane was employed as the separator, and each cell was filled with 80 μL of 3 M $Zn(CF_3SO_3)_2$ aqueous electrolyte. Cyclic voltammetry (CV) was conducted on a CHI 760E electrochemical workstation (Chenhua, Shanghai, China). Electrochemical impedance spectroscopy (EIS) measurements were performed over the frequency range of 100 kHz to 0.01 Hz using an amplitude of 5 mV. Galvanostatic charge/discharge measurements and galvanostatic intermittent titration technique (GITT) analyses were carried out on a Neware battery testing system (CT-4008, Neware, Shenzhen, China).

3. Results and Discussion

X-ray diffraction (XRD) was employed to characterize the crystal structures of the as-prepared samples. As shown in Figure 1a, the diffraction peaks of VOH agree well with the standard reference pattern (PDF No. 40-1296). The diffraction pattern of BVOH can be indexed to a different reference pattern (PDF No. 45-1326), suggesting a structural transformation induced by $BMIM^+$ incorporation. Both VOH and BVOH exhibit characteristic low-angle diffraction peaks associated with the (001) plane of layered vanadium oxides, indicating that the original two-dimensional layered framework is well preserved after cation pre-intercalation. As revealed in the magnified inset, VOH displays a (001) reflection at approximately 7.5°, corresponding to an interlayer spacing of 11.7 Å. After $BMIM^+$ pre-intercalation, the (001) peak of BVOH shifts to a lower 2θ value of 7.04°, accompanied by an expansion of the interlayer spacing to 12.9 Å. This shift confirms the successful incorporation of $BMIM^+$ cations into the interlayer galleries of the vanadium oxide framework. The pre-intercalated cations effectively enlarge the interlayer channels, thereby providing more spacious pathways for Zn^{2+} transport and facilitating its solid-state diffusion within the layered host. Fourier-transform infrared spectroscopy (FT-IR) was used to identify functional groups and chemical compositions of the samples (Figure 1b). Compared with pristine VOH, BVOH exhibits additional characteristic absorption bands in the 1300–1500 cm^{-1} region, which are assigned to the C-N stretching vibrations of the imidazolium ring, confirming the successful incorporation of $BMIM^+$ cations into the VOH framework [27]. Meanwhile, distinct shifts are observed in the characteristic vibrational bands associated with the vanadium-oxygen framework. Specifically, the vibration of terminal V^{5+}=O bonds shifts to higher wavenumbers, whereas the bridging V-O-V vibration shifts toward lower wavenumbers [28]. The blue shift of the terminal V^{5+}=O band may be associated with changes in the vanadium oxidation-state distribution, whereas the red shift of the bridging V-O-V band may arise from changes in bond geometry and local lattice distortion. These results suggest that imidazolium cation incorporation modifies the electronic and structural environment of the vanadium oxide layers [29]. Raman spectroscopy was further employed to elucidate the structural evolution induced by $BMIM^+$ pre-intercalation (Figure 1c). Compared with VOH, BVOH exhibits additional Raman features in the 1500–1700 cm^{-1} region, which can be assigned to the conjugated C=C and C=N vibrations of the imidazolium ring, confirming the stable incorporation of the organic cations within the interlayer galleries. The Raman bands centered at 154, 271, 336, 520, and 691 cm^{-1} are attributed to the vibrational modes of O-V-O, V=O, H_2O, V_3-O, and V_2-O, respectively. Notably, the V_3-O vibration undergoes a red shift after $BMIM^+$ intercalation, suggesting a weakened V-O bonding interaction and a distortion of the local [VO_6] octahedral coordination environment [30,31]. In addition, the intensities of characteristic peaks originating from interlayer water decrease, which proves that the hydrophobic butyl side chains can effectively repel excessive interlayer water molecules.

Figure 1d presents the high-resolution V 2p X-ray photoelectron spectroscopy (XPS, Thermo Scientific, Waltham, MA, USA) spectra of VOH and BVOH. The spectra of both samples can be deconvoluted into characteristic components associated with V^{5+} and V^{4+} species [32]. Notably, the V^{5+}/V^{4+} ratio decreases from 3.99 for VOH to 1.66 after $BMIM^+$ pre-intercalation, indicating an increase in the proportion of reduced V^{4+} species. This change suggests that the incorporation of $BMIM^+$ cations induces a redistribution of the local electronic structure within the vanadium oxide framework, which is associated with the formation of oxygen vacancies. The increased concentration of V^{4+} and oxygen vacancies may enhance the electronic conductivity, thereby benefiting Zn^{2+} storage kinetics. In the high-resolution O 1s spectra of BVOH (Figure 1e), three components are assigned to hydroxyl oxygen (O-H), oxygen vacancy (O_v), and lattice V-O bonds, respectively [33]. Compared with VOH,

BVOH exhibits a reduced contribution from the O-H component, accompanied by a new O_v signal. The decreased O-H content is consistent with the hydrophobic character of the butyl substituents, which is expected to reduce the amount of interlayer water. In addition, the N 1s and C 1s XPS spectra provide further evidence for the successful incorporation of $BMIM^+$ cations into the VOH framework (Figures S1 and S2). Thermogravimetric analysis coupled with differential scanning calorimetry (TG-DSC) was employed to examine the thermal evolution of the samples (Figure 1f). For VOH, the initial mass loss below approximately 150 °C is attributed to the removal of physically adsorbed water. A subsequent weight-loss process between approximately 150 and 320 °C is associated with the progressive release of interlayer water, accompanied by structural rearrangement of the hydrated vanadium oxide framework [34]. In contrast, BVOH exhibits an additional mass-loss region spanning approximately 250–400 °C, together with a distinct thermal event in the DSC profile. This feature is assigned to the thermal decomposition of the intercalated $BMIM^+$ species, providing further evidence for their successful incorporation within the VOH interlayers. Based on the mass-loss profiles obtained from TG analysis, the V^{5+}/V^{4+} ratios determined by XPS and the principle of charge neutrality, the chemical formulas of VOH and BVOH were estimated to be $V_2O_5 \cdot 0.7H_2O$ and $BMIM_{0.15}V_2O_{4.7} \cdot 0.47H_2O$, respectively. As revealed by scanning electron microscopy (SEM) (Figure 1g), BVOH exhibits a continuous and interconnected three-dimensional porous network architecture, in contrast to the 2D sheet-like structure of VOH (Figure S3). At higher magnification (Figure 1h), the nanosheets of BVOH appear to be well separated and interconnected, with limited restacking or aggregation. Such an expanded nanosheet architecture provides abundant accessible surfaces and interconnected ion-transport pathways, facilitating electrolyte/electrode interfacial contact and potentially accelerating Zn^{2+} diffusion and migration within the electrode. Transmission electron microscopy (TEM) further reveals the ultrathin and curled nanosheet morphology of BVOH (Figure 1i). The interlayer spacing along the (001) direction is measured to be 12.9 Å, in good agreement with the value derived from the XRD results, corroborating the successful expansion of the layered structure. The high-resolution TEM (HRTEM) image (Figure S4) displays localized lattice distortions and dislocations within the crystal domains, suggesting the presence of structural defects associated with oxygen-vacancy formation. The selected area electron diffraction (SAED) pattern further confirms the crystalline nature of BVOH (Figure S5). In addition, energy-dispersive X-ray spectroscopy (EDS) elemental mapping reveals a homogeneous distribution of V, O, C, and N throughout the nanosheets (Figure S6), providing further evidence for the uniform incorporation of $BMIM^+$ cations within the VOH framework.

The cyclic voltammetry (CV) profiles of the VOH and BVOH electrodes over the initial three cycles at a scan rate of 0.1 mV s^{-1} are displayed in Figure 2a and Figure S7. Compared with VOH, BVOH exhibits an improved overlap of the redox peaks in terms of both potential position and peak shape, indicating enhanced electrochemical reversibility after $BMIM^+$ pre-intercalation. Two distinct pairs of redox peaks are observed for both electrodes, which can be assigned to the reversible multistep redox reactions of vanadium during Zn^{2+} storage. Notably, BVOH delivers higher peak current densities and smaller voltage gaps, suggesting more favorable reaction kinetics and ion-storage capability (Figure S8). Figure 2b presents the galvanostatic charge/discharge (GCD) profiles of VOH and BVOH at 0.1 A g^{-1}. The voltage plateaus in both electrodes are consistent with the redox features identified from the corresponding CV curves, indicating that the electrochemical reactions are largely preserved after interlayer modification. Notably, BVOH exhibits a reduced potential gap between the charge and discharge profiles and a higher open-circuit potential (OCP) of 1.6 V (Zn^{2+}/Zn) after resting for 2 h compared with VOH, indicative of diminished electrochemical polarization and improved reaction reversibility. The higher OCP of BVOH may be attributed to $BMIM^+$-induced modulation of the V-O electronic environment, as supported by the altered V^{5+}/V^{4+} ratio observed in XPS, which may lower the cathode electron electrochemical potential and increase the voltage difference relative to the Zn anode. In addition, BVOH delivers a discharge capacity of 452 mAh g^{-1} (an areal capacity of 0.76 mAh cm^{-2}), exceeding the 321 mAh g^{-1} (an areal capacity of 0.26 mAh cm^{-2}) obtained for VOH. The rate capability of the two electrodes was evaluated over a wide current density range of 0.5–10 A g^{-1} (Figure 2c). BVOH delivers average discharge capacities of 403, 377, 353, 310, 271, and 247 mAh g^{-1} at 0.5, 1, 2, 5, 8, and 10 A g^{-1}, respectively. Upon returning the current density to 0.5 A g^{-1}, the capacity rapidly recovers to 378 mAh g^{-1}, indicating highly reversible electrochemical kinetics with limited structural or interfacial degradation during rate cycling. In comparison, VOH exhibits lower capacities throughout all current densities, highlighting the enhanced high-rate response afforded by the BVOH structure. The corresponding GCD profiles (Figure S9) show well-defined discharge/charge features with only modest polarization as the current density increases, further supporting the favorable charge-transfer kinetics of BVOH. As shown in the Ragone plots (Figure 2d), the Zn||BVOH cell delivers an energy density of 338 Wh kg^{-1} at a power density of 463 W kg^{-1}. Notably, even when the power density increases to 7880 W kg^{-1}, the cell maintains an energy density of 181 Wh kg^{-1}, higher than other reported cathodes [35–43].

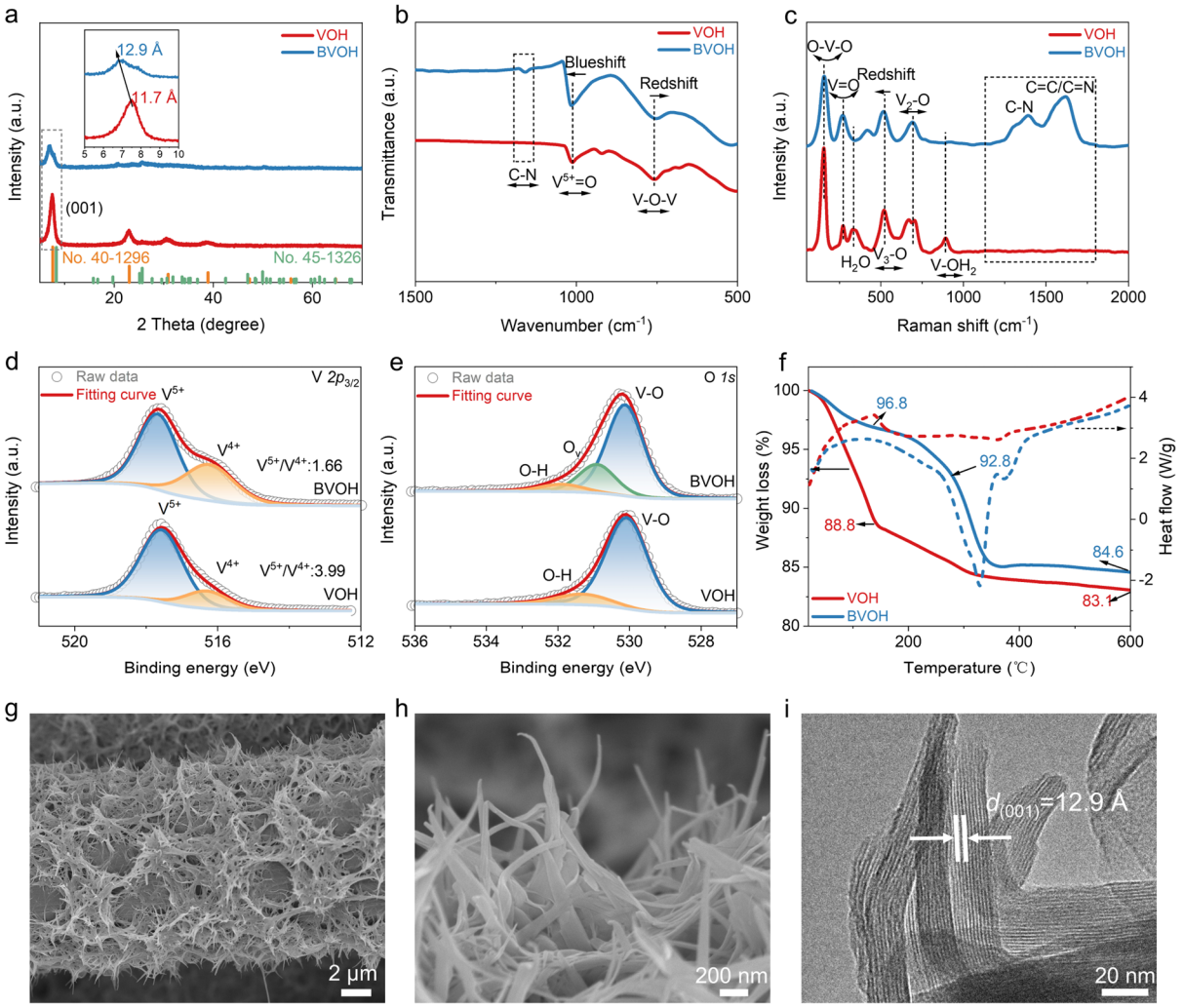


Figure 1. Structure and chemical environment of VOH and BVOH. (**a**) XRD patterns. (**b**) FTIR spectra. (**c**) Raman spectra. High-resolution XPS spectra of (**d**) V 2p3/2 and (**e**) O 1s. (**f**) Combined TG-DSC curves. (**g**) SEM image of BVOH. (**h**) High-magnification SEM of BVOH. (**i**) TEM image of BVOH.

Self-discharge behavior was assessed to evaluate the electrochemical stability of the electrodes during the resting period (Figure 2e). After being charged to 1.6 V and subsequently held at open circuit for 48 h, the Zn||BVOH cell maintains an OCV of 1.3 V and recovered 90% of its initial discharge capacity. In contrast, the Zn||VOH cell exhibits an obvious voltage decay to 1.08 V and retained only 64.8% of its initial capacity. The suppressed self-discharge of BVOH indicates that $BMIM^+$ intercalation mitigates parasitic reactions and active-material loss at the electrode/electrolyte interface. This stabilization may be attributed to the hydrophobic alkyl chains of the intercalated $BMIM^+$ cations. As supported by the water contact-angle measurements (Figure S10), BVOH exhibits reduced surface wettability compared with VOH, which may limit direct water contact with reactive surface sites, thereby mitigating water-related parasitic reactions during the resting period. The cycling stability was evaluated at 0.5 A g^{-1} (Figure 2f). BVOH retained 88.4% of its initial capacity after 200 cycles, while maintaining a Coulombic efficiency close to 100%. By comparison, the capacity of VOH rapidly deteriorated, with only 41.5% retention. The long-term cycling behavior was further examined at an ultrahigh current density of 8 A g^{-1} (Figure 2g). Even after 8000 cycles, BVOH preserved 90.3% of its initial capacity, with the Coulombic efficiency remaining ~100% throughout the measurement. In comparison, VOH retained only 45.7% of its initial capacity under identical conditions. The poor performance of bare VOH arises from continuous layered framework collapse and massive vanadium dissolution upon repeated cycling. The pre-intercalated $BMIM^+$ cations provide persistent interlayer support, helping maintain the structural integrity of the host lattice over prolonged cycling, while the hydrophobic alkyl groups reduce the contact between the active framework and aqueous electrolyte, thereby suppressing vanadium dissolution. These results validate that this modification strategy is applicable for high-power energy storage systems requiring ultra-long service life. To explore the practical applicability of BVOH in practical devices, a pouch cell employing BVOH as the cathode was assembled for electrochemical performance evaluation (Figure 2h). The pouch cell delivered an initial discharge capacity of 354 mAh g^{-1} and

retained 321 mAh g^{-1} after 350 cycles, with ~100% Coulombic efficiency. Digital photographs show that this pouch cell delivers a stable open-circuit voltage of 1.571 V and continuously powered a small fan, demonstrating its ability to provide a stable electrical output under practical conditions.

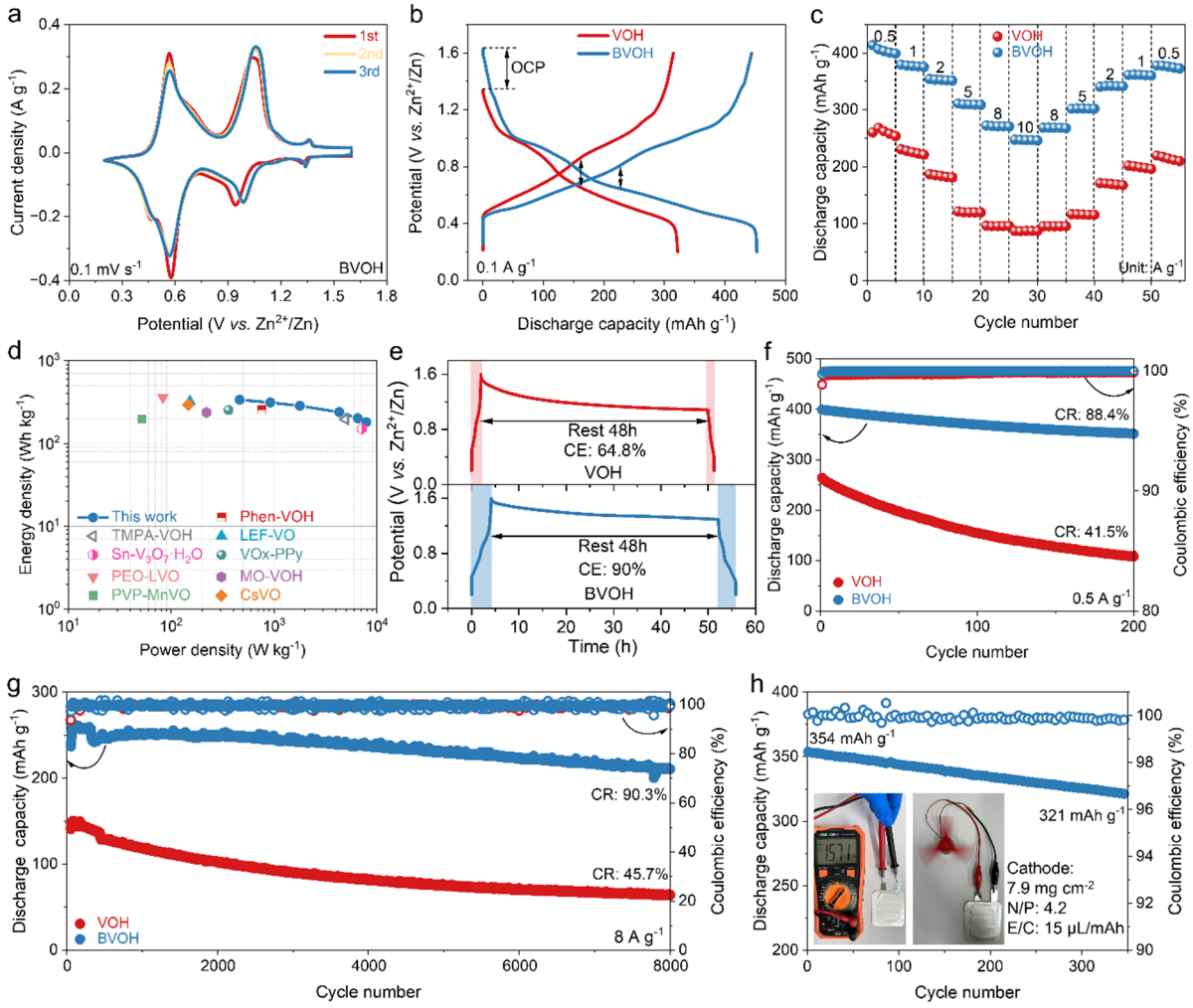


Figure 2. Electrochemical properties of VOH and BVOH. (**a**) CV curves at 0.1 mV s^{-1}. (**b**) Voltage profiles at 0.1 A g^{-1}. (**c**) Rate performance. (**d**) Ragone plots. (**e**) Self-discharge tests after resting for 48 h. Cycle stability at (**f**) 0.5 A g^{-1} and (**g**) 8 A g^{-1}. (**h**) Cycling performance of Zn||BVOH pouch cell; inset shows photographs of the assembled soft-pack battery powering a fan.

Figure 3a presents the CV profiles of the BVOH electrode recorded at scan rates ranging from 0.2 to 1.2 mV s^{-1}. The shape of the CV curves is well preserved with increasing scan rate, indicating highly reversible redox behavior. Meanwhile, the anodic and cathodic peaks gradually shift toward higher and lower potentials, respectively, owing to the increased electrode polarization at faster scan rates. To further elucidate the charge storage kinetics, the relationship between the peak current (i) and scan rate (v) was analyzed according to $i = av^b$, where the b value reflects the dominant charge storage mechanism [44,45]. As shown in Figure 3b, the b values for peaks A, B, C, and D are 1.00, 0.71, 0.88, and 0.83, respectively, revealing the coexistence of diffusion-controlled behavior and surface-capacitive processes. The kinetics of BVOH is further evidenced by the quantitative separation of capacitive and diffusion-controlled contributions. At 0.5 mV s^{-1}, the capacitive contribution reaches 74% for BVOH (Figure S11), higher than that of VOH (68%), indicative of faster electrochemical response kinetics. With increasing scan rate from 0.2 to 1.2 mV s^{-1}, the capacitive contribution increases from 63% to 93% (Figure 3c), demonstrating the increasingly dominant role of rapid surface-controlled Zn^{2+} storage under high rate operation. Such a pseudocapacitive character provides an important kinetic basis for the superior rate capability of BVOH. In comparison, VOH exhibits lower b values and capacitive contributions, suggesting more sluggish kinetics (Figures S12–S14). The Zn^{2+} diffusion kinetics within the electrodes were quantitatively evaluated by galvanostatic intermittent titration technique (GITT), as shown in Figure S15. Across the entire Zn^{2+} intercalation/deintercalation process, the BVOH electrode exhibits diffusion coefficients in the range of 10^{-9}–10^{-11}

$cm^2\ s^{-1}$, higher than those of VOH (10^{-10}–10^{-12} $cm^2\ s^{-1}$), demonstrating accelerated solid-state Zn^{2+} transport in BVOH (Figure 3d). Such kinetic improvement is associated with the pre-intercalated $BMIM^+$, which enlarge the interlayer spacing and maintain more accessible ion-transport pathways. In addition, the positively charged imidazolium groups modify the electrostatic environment within the interlayer galleries, thereby alleviating the electrostatic interactions between hydrated Zn^{2+} and the vanadium oxide host and facilitating Zn^{2+} migration.

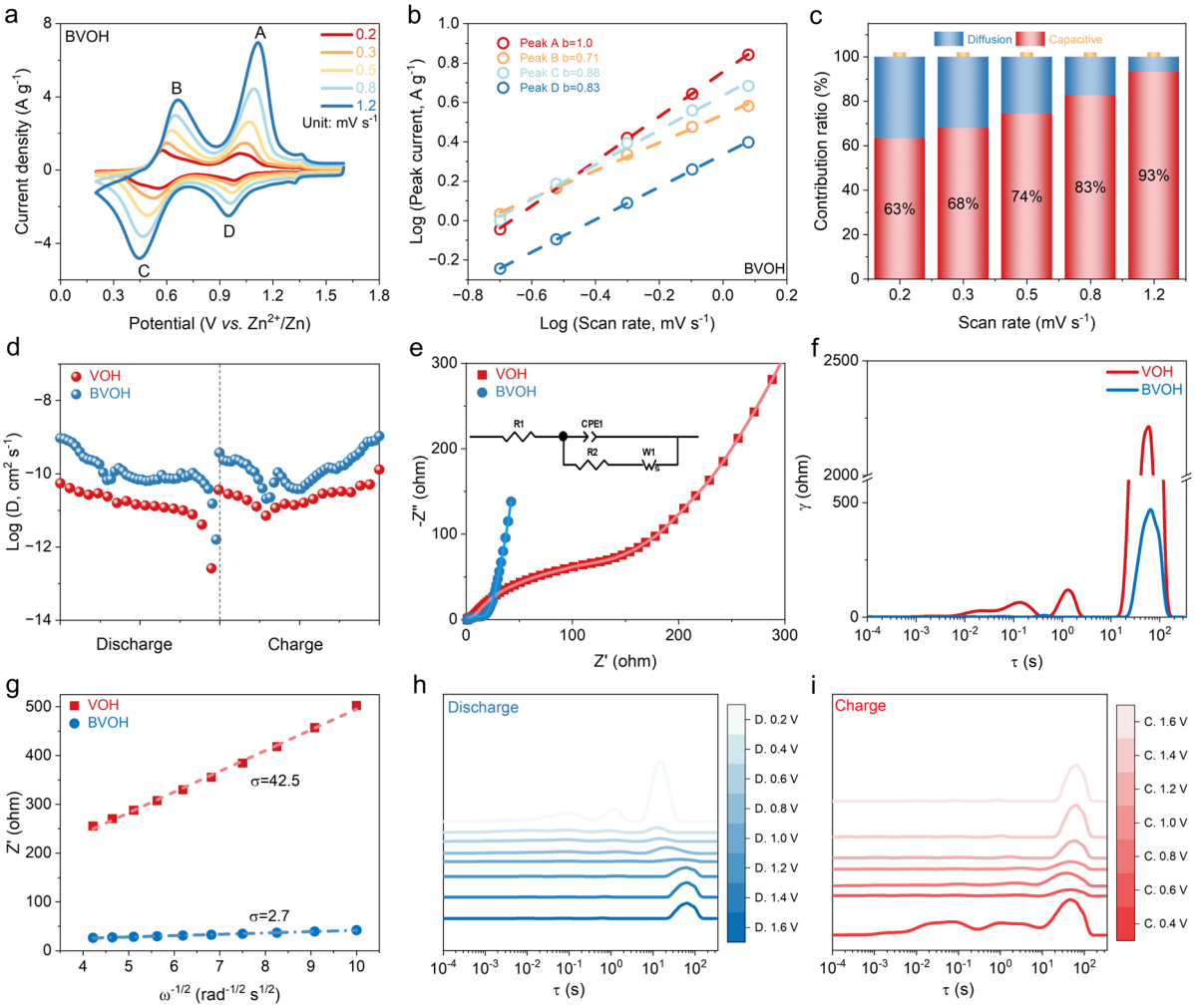


Figure 3. Electrochemical kinetic analysis of VOH and BVOH electrodes. (**a**) CV curves of BVOH at various scan rates. (**b**) Corresponding Log(i) vs. log(v) plots. (**c**) Capacitive and diffusion-controlled contribution ratios at different scan rates. (**d**) Zn^{2+} diffusion coefficients calculated from GITT results. (**e**) Nyquist plots of VOH and BVOH. (**f**) DRT spectra derived from EIS data. (**g**) Linear fitting of Z' against $\omega^{-1/2}$ for obtaining the Warburg factor. *In situ* DRT contour plots of BVOH during (**h**) discharge and (**i**) charge processes.

The interfacial reaction kinetics were further examined by electrochemical impedance spectroscopy (EIS) (Figure 3e). BVOH exhibits a smaller charge-transfer resistance (R_{ct}) than VOH, indicating faster electrode/electrolyte interfacial kinetics. This improvement can be attributed to the defect-rich structure generated during the pre-intercalation process, as oxygen vacancies enhance the electronic conductivity of the vanadium oxide framework. To further deconvolute the individual kinetic contributions, the EIS responses were analyzed using the distribution of relaxation times (DRT) method (Figure 3f). The DRT method decouples impedance signals on the time scale and distinguishes diverse electrochemical processes including four characteristic relaxation processes at approximately 0.01, 0.1, 1, and 10–100 s, which are assigned to surface adsorption (R_{ads}), interfacial ion migration/desolvation (R_{mig}), charge transfer (R_{ct}), and solid-state Zn^{2+} diffusion (R_{diff}), respectively [46,47]. Compared with VOH, the BVOH electrode displays weakened DRT features together with shorter characteristic relaxation times, indicating suppressed polarization and accelerated reaction kinetics across multiple time scales. In particular, the reduced relaxation times associated with interfacial ion migration and charge transfer suggest more facile Zn^{2+} transport across the electrode/electrolyte interface, whereas the attenuated low-frequency response reflects improved solid-state ion diffusion within the cathode. In addition, the low-frequency region of

the EIS spectra exhibits the characteristic Warburg response associated with Zn^{2+} diffusion in the solid phase [48]. Notably, BVOH delivers a σ value of only 2.7, substantially lower than that of VOH (42.5), further confirming the significantly reduced diffusion resistance after $BMIM^+$ pre-intercalation (Figure 3g). Taken together, $BMIM^+$ pre-intercalation promotes interfacial charge transfer and solid-state Zn^{2+} migration, accounting for the enhanced electrochemical kinetics of BVOH. To gain deeper insight into the charge/discharge kinetics, *in situ* DRT analysis was performed on the assembled coin cells. During discharge (Figure 3h), the characteristic relaxation time in the low-frequency region initially decreases, indicating an acceleration of the electrochemical kinetics. This evolution occurs between 0.8 and 0.2 V, where H^+ insertion becomes dominant. Owing to its small ionic radius and high mobility, H^+ can undergo rapid interfacial transfer and diffusion within the host structure, thereby accelerating the electrode reaction and shortening the corresponding characteristic time. During the charging process (Figure 3i), the short characteristic time as the voltage rises from 0.2 to 0.8 V corresponds to the H^+ extraction region. Upon further charging above 0.8 V, the characteristic time gradually increases toward the end of charge. This kinetic deceleration is consistent with the Zn^{2++} extraction. Compared with H^+, the extraction of the larger divalent Zn^{2+} ions involves a higher migration barrier and more pronounced structural reorganization of the host lattice, resulting in slower reaction kinetics. These results reveal distinct kinetic responses associated with the insertion/extraction of H^+ and Zn^{2+} during the electrochemical process.

The charge-storage mechanism of BVOH was elucidated by tracking the structural and local bonding evolution throughout the initial electrochemical cycle. *Ex situ* XRD patterns (Figure 4a) show that the characteristic reflections of BVOH are largely preserved during cycling, although their intensities vary, demonstrating the robust structural integrity of the layered framework. During discharge, an additional diffraction peak emerges at 13.4° and disappears upon subsequent charging. The reversible diffraction peak appearing at approximately 13.4° during the early discharge stage can be assigned to the (002) plane of $Zn_x(CF_3SO_3)_y(OH)_{2x-y}{\cdot}nH_2O$ (BZS), suggesting that BZS formation may occur early in the discharge process due to a local increase in interfacial pH [49]. This result is further consistent with the kinetic information obtained from the *in situ* EIS measurements. Meanwhile, the characteristic (001) reflection gradually weakens and shifts toward higher 2θ values upon discharge, indicating a reversible contraction of the interlayer galleries during insertion. Upon subsequent charging, the peak returns toward lower angles and eventually approaches its initial state, demonstrating the recovery of the layered framework. To directly visualize these structural changes at the atomic scale, *ex situ* HRTEM measurements were further performed on the electrodes at the fully discharged and fully charged states (Figure 4b). The interlayer spacing decreases reversibly from 12.9 Å in the pristine state to 12.2 Å after full discharge, followed by complete recovery to 12.9 Å upon subsequent charging. These results provide direct evidence for the highly reversible breathing behavior of the BVOH interlayers during charge storage, highlighting the structural adaptability conferred by imidazolium-cation pre-intercalation. Figure 4c presents the *ex situ* high-resolution V $2p_{3/2}$ spectra of BVOH at the discharged and charged states, revealing reversible changes in the vanadium oxidation states during Zn^{2+} storage. Upon discharge, an increase in the V^{3+} contribution indicates the reduction of vanadium species during the insertion process. After charging, the V^{3+} signal disappears, while the spectral features recover to the coexistence of V^{4+} and V^{5+}, demonstrating the reversible oxidation of the reduced vanadium species upon Zn^{2+} extraction. The higher V^{4+} fraction associated with trapped Zn^{2+} enhances electronic transport, while the retained Zn^{2+} ions serve as structural pillars that stabilize the host framework. These reversible valence variations confirm that the Zn^{2+} storage process in BVOH is primarily governed by the multielectron redox activity of vanadium. The high-resolution Zn 2p spectra (Figure 4d) directly track the reversible insertion and extraction of Zn^{2+}. Strong Zn 2p signals emerge in the fully discharged state, confirming substantial accumulation of Zn^{2+} within the layered host. Upon recharging, the intensity of both Zn 2p peaks decreases, indicating the effective removal of the inserted Zn^{2+}. The morphological evolution of the electrode at the fully discharged and charged states is compared in Figure 4e. Upon discharge, when Zn^{2+} is intercalated into the layered structure, additional flake-like deposits are observed on the surface of the nanobelts, which is attributed to the BZS byproducts. These features disappear after charging, with the nanobelt morphology largely recovered, indicating that the structural changes are highly reversible. Elemental mapping of the discharged and charged electrodes (Figure 4f,g) further reveals a homogeneous distribution of V, O, C, and N throughout both states. The C and N signals originate from the pre-intercalated $BMIM^+$ cations residing between the vanadium oxide layers, which are retained during Zn^{2+} insertion/extraction. In contrast, the Zn signal is enhanced in the discharged state. After charging, the Zn signal decreases, consistent with the reversible extraction of Zn^{2+} from the interlayer region. This trend is consistent with XPS results, further verifying the reversible intercalation and deintercalation behavior of Zn^{2+} in BVOH.

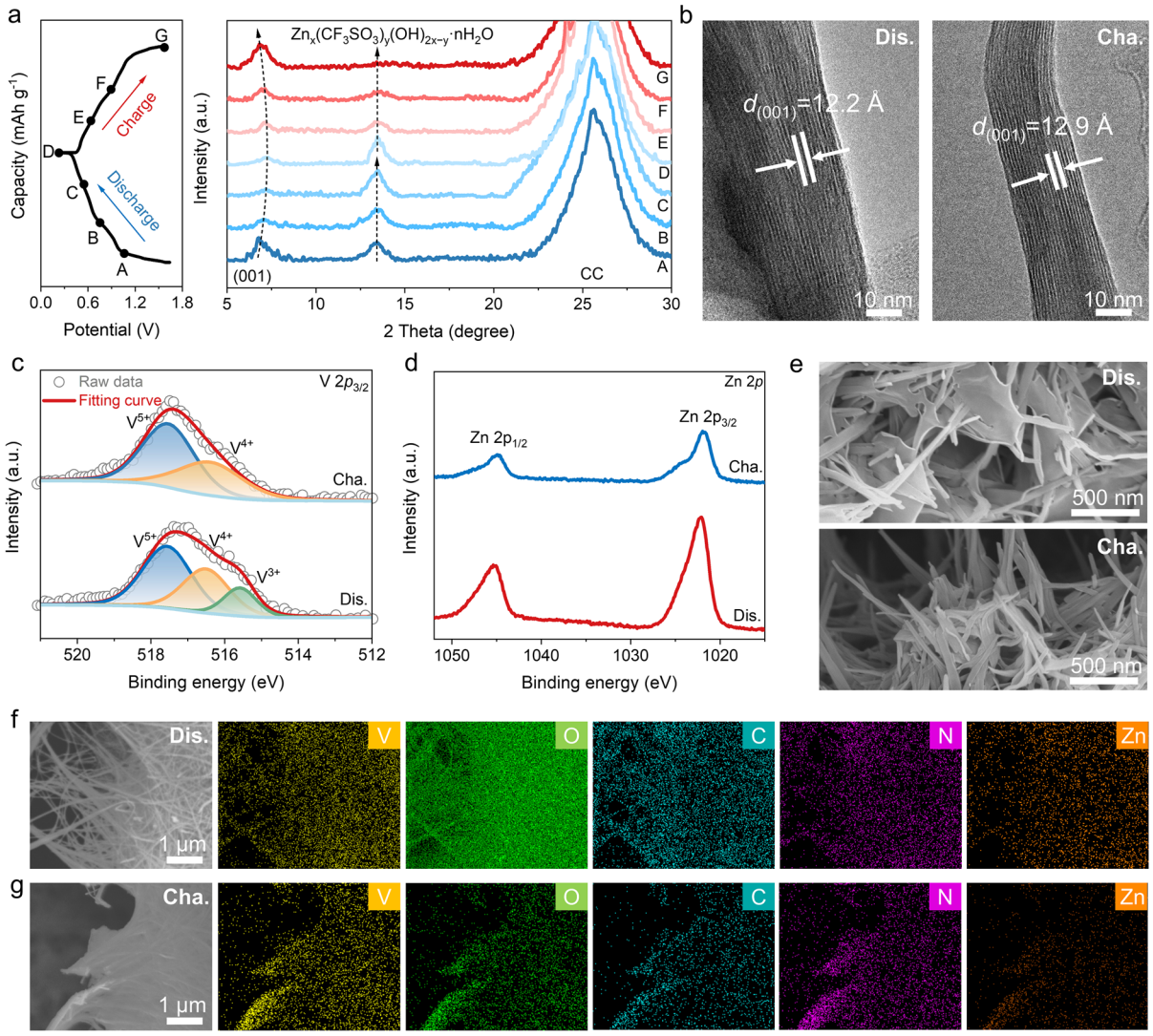


Figure 4. *Ex situ* characterizations of charge storage mechanism. (**a**) *Ex situ* XRD patterns at representative discharge/charge states. (**b**) HRTEM images of fully discharged (Dis.) and fully charged (Cha.) BVOH. High-resolution XPS spectra of (**c**) V $2p_{3/2}$ and (**d**) Zn 2p for discharged and charged electrodes. (**e**) SEM images of BVOH at fully discharged and charged states. EDS elemental mapping of V, O, C, N and Zn for BVOH at (**f**) discharged state and (**g**) charged state.

First-principles calculations were further performed to elucidate how pre-intercalated $BMIM^+$ regulates the local electronic structure, interlayer electrostatic environment, and Zn^{2+} migration kinetics at the atomic scale (Figure S16). Figure 5a,b present the charge density difference maps of VOH and BVOH after Zn^{2+} insertion, respectively, where the yellow and cyan regions denote charge accumulation and depletion [50]. In VOH, charge redistribution occurs at the interface, with electron density rearrangement extending across both adjacent VO frameworks. This electronic coupling indicates a strong interaction between the inserted Zn^{2+} and the surrounding vanadium oxide framework, which may impose a considerable energetic constraint on Zn^{2+} migration. By contrast, the charge redistribution associated with Zn^{2+} insertion is altered in BVOH. The presence of interlayer $BMIM^+$ redistributes the electronic response of the host lattice, and the charge density perturbation induced by Zn^{2+} becomes weak at the interface. Notably, the charge redistribution is partially localized around the interlayer region, suggesting that the pre-intercalated organic cations modulate the local electrostatic coupling between Zn^{2+} and the vanadium oxide layer. In particular, the interaction between Zn^{2+} and one side of the VO framework is effectively attenuated, thereby reducing the interfacial binding strength that can hinder ion migration [51]. This interlayer environment is expected to facilitate Zn^{2+} insertion/extraction and accelerate solid-state ion transport during repeated cycling. The electrostatic potential (ESP) distribution of the $BMIM^+$ cation further provides insight into its role in regulating the local interlayer environment (Figure 5c). The imidazolium ring exhibits a highly polarized electrostatic distribution, with localized electron-rich regions around the N sites. Such an inhomogeneous charge distribution can provide additional favorable environments for guest Zn^{2+} and modulate their local structural and

electronic environment. Meanwhile, the relatively nonpolar butyl moiety interacts more weakly with Zn^{2+} and introduces steric separation within the interlayer space. The synergistic combination of localized electrostatic interactions and steric regulation therefore prevents strong Zn^{2+} binding while maintaining accessible migration pathways, enabling more reversible ion transport.

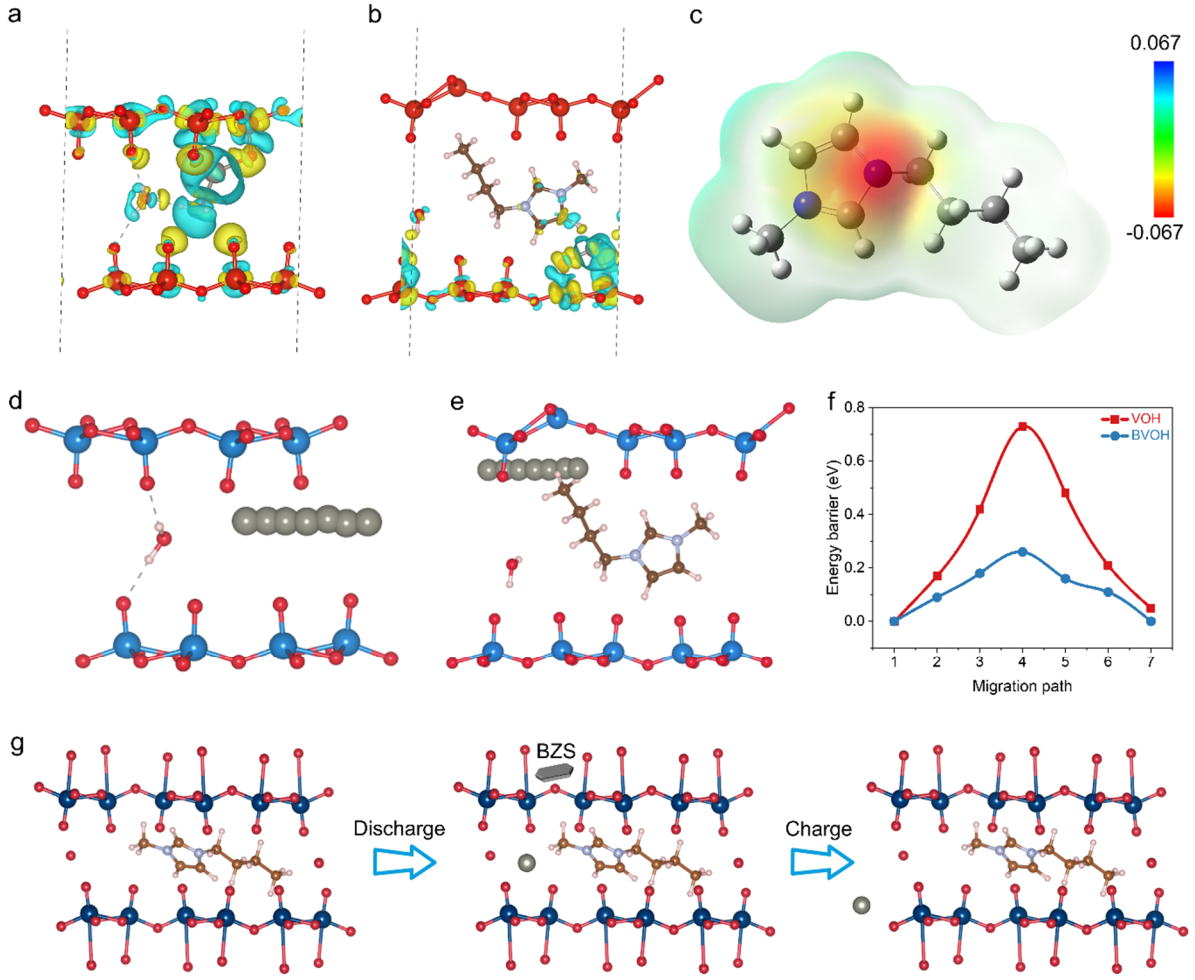


Figure 5. Theoretical calculation results. Charge density difference plots of (**a**) VOH and (**b**) BVOH. (**c**) ESP distribution of $BMIM^+$. Zn^{2+} migration models in (**d**) VOH and (**e**) BVOH. (**f**) Energy barrier profiles for Zn^{2+} migration in VOH and BVOH. (**g**) Schematic illustration of reversible Zn^{2+} intercalation/deintercalation mechanism in BVOH during discharge and charge processes.

To quantitatively evaluate the effect of $BMIM^+$ on Zn^{2+} transport, the diffusion pathways and corresponding migration energy profiles were further calculated using density functional theory (DFT) (Figure 5d,e). The Zn migration barrier decreases substantially from 0.73 eV in VOH to only 0.26 eV in BVOH (Figure 5f), demonstrating a fast reaction kinetics after $BMIM^+$ pre-intercalation. This reduction can be ascribed to the combined effects of interlayer expansion and local electrostatic regulation. On the one hand, the enlarged interlayer spacing provides a more spacious diffusion corridor for Zn^{2+} migration. On the other hand, the polarized $BMIM^+$ species partially screens the strong electrostatic interaction between Zn^{2++} and the lattice oxygen atoms, thereby flattening the migration energy landscape. The defect-rich structure introduced during cation pre-intercalation may further provide additional accessible pathways for ion transport. Together, these effects account for the reduced migration barrier and enhanced Zn^{2+} diffusion kinetics in BVOH. Based on the experimental results and theoretical calculations, a structural evolution mechanism for BVOH during Zn^{2+} storage is proposed (Figure 5g). In the pristine state, $BMIM^+$ cations are stably confined between adjacent vanadium oxide layers, where they function as interlayer spacers and regulate the local chemical and electrostatic environment. During discharge, Zn^{2+} reversibly inserts into the expanded galleries and participates in the redox reaction of the vanadium-oxygen framework, accompanied by the formation of BZS intermediates. The enlarged interlayer channels, abundant oxygen vacancies, and optimized electronic environment promote ion diffusion and charge transfer. Upon charging, Zn^{2+} is extracted while the pre-intercalated $BMIM^+$ remains anchored within the lattice, preserving the expanded

interlayer framework and mitigating irreversible layer contraction during repeated cycling. Such persistent interlayer regulation stabilizes the host structure and lowers the kinetic barrier for Zn^{2+} transport, ultimately resulting in the high reversible capacity, excellent rate capability, and long-term cycling stability of BVOH.

4. Conclusions

In summary, we demonstrate an ionic-liquid cation pre-intercalation strategy for reconstructing the interlayer microenvironment of hydrated vanadium pentoxide toward durable and high-rate aqueous ZIBs. By introducing $BMIM^+$ into the VOH framework, the functionalities of the organic cation are exploited to address the instability and sluggish ion transport of VOH. The $BMIM^+$ acts as a molecular pillar to expand the interlayer spacing and preserve an open ion-transport framework, while its hydrophobic butyl chain partially regulates the interlayer water environment and mitigates water-mediated structural degradation. Meanwhile, the polar imidazolium moiety reconstructs the local electrostatic environment and provides additional favorable environments for Zn^{2+} storage. Beyond these interlayer effects, $BMIM^+$ pre-intercalation induces oxygen vacancies, enhances electronic conductivity, and lowers the Zn^{2+} migration barrier, accelerating charge-transfer and ion-transport kinetics. As a result, BVOH delivers high reversible capacity, excellent rate capability, and outstanding long-term cycling stability. This work highlights the broader potential of organic cation pre-intercalation for regulating interlayer structure and charge-storage kinetics, offering an effective strategy for designing high-performance layered metal oxide cathodes for aqueous ZIBs.

Supplementary Materials

The additional data and information can be downloaded at: https://media.sciltp.com/articles/others/2611131437426904/eChem-26090110-SI.pdf. Refs. [52–59] are cited in the Supplementary Materials.

Author Contributions

Y.J.: Conceptualization, Data Curation, Investigation, Writing—original draft; H.J.: Investigation, Data Curation, Formal Analysis; K.C.: Methodology, Investigation, Data Curation; Z.L.: Investigation, Data Curation; D.C.: Supervision; Q.K.: Resources; Q.Z.: Funding Acquisition, Conceptualization, Supervision, Writing—Review & Editing. All authors have read and agreed to the published version of the manuscript.

Funding

This work was supported by the National Natural Science Foundation of China (Grant No. 52302322) and Zhejiang Provincial Natural Science Foundation of China (Grant No. LQ24E020004).

Institutional Review Board Statement

Not applicable.

Informed Consent Statement

Not applicable.

Data Availability Statement

The data supporting the findings of this study are available within the article and its Supporting Information. Additional data are available from the corresponding author upon reasonable request.

Conflicts of Interest

The authors declare no conflict of interest.

Use of AI and AI-Assisted Technologies

The authors used ChatGPT (OpenAI) for language polishing. After using this tool, the authors carefully reviewed and take full responsibility for the content of the published article.

References

1. Zhu, Z.; Jiang, T.; Ali, M.; et al. Rechargeable Batteries for Grid Scale Energy Storage. *Chem. Rev.* **2022**, *122*, 16610–16751. https://doi.org/10.1021/acs.chemrev.2c00289.
2. Jiang, T.; Shen, D.; Zhang, Z.; et al. Battery technologies for grid-scale energy storage. *Nat. Rev. Clean Technol.* **2025**, *1*, 474–492. https://doi.org/10.1038/s44359-025-00067-9.
3. White, M.; Choi, M.; Hu, B.; et al. Recent Advances in Scalable, High-Mass Loaded Electrodes for Grid-Scale Energy Storage. *Adv. Mater.* **2025**, *37*, 2417128. https://doi.org/10.1002/adma.202417128.
4. Mu, X.; Pan, H.; He, P.; et al. Li–CO_2 and Na–CO_2 Batteries: Toward Greener and Sustainable Electrical Energy Storage. *Adv. Mater.* **2020**, *32*, 1903790. https://doi.org/10.1002/adma.201903790.
5. Huang, Y.; Li, J. Key Challenges for Grid-Scale Lithium-Ion Battery Energy Storage. *Adv. Energy Mater.* **2022**, *12*, 2202197. https://doi.org/10.1002/aenm.202202197.
6. Khan, A.; Al Rashid, H.; Roy, P.K.; et al. Challenges and the Way to Improve Lithium-Ion Battery Technology for Next-Generation Energy Storage. *Energy Environ. Mater.* **2025**, *8*, e70088. https://doi.org/10.1002/eem2.70088.
7. Yang, X.; Zhang, H.; Liu, Q.; et al. The Li-ion battery industry and its challenges. *Nat. Rev. Chem.* **2025**, *9*, 497–498. https://doi.org/10.1038/s41570-025-00742-2.
8. Roy, J.J.; Phuong, D.M.; Verma, V.; et al. Direct recycling of Li-ion batteries from cell to pack level: Challenges and prospects on technology, scalability, sustainability, and economics. *Carbon Energy* **2024**, *6*, e492. https://doi.org/10.1002/cey2.492.
9. Gong, X.; Wang, Y.; Ge, M.; et al. Polyaniline-Modified MXene/Carbon Nanotube Scaffold Enabling High-Rate and Long-Cycle Zinc–Iodine Batteries. *Nano Lett.* **2026**, *26*, 14462–14470. https://doi.org/10.1021/acs.nanolett.6c04159.
10. Hu, X.; Lai, G.; Liu, Y.; et al. Design of dual-electrode interfacial kinetics regulator for long-lasting Ah-level zinc-iodine batteries. *eScience* **2025**, *5*, 100455. https://doi.org/10.1016/j.esci.2025.100455.
11. Liu, S.; Zhang, R.; Wang, C.; et al. Zinc ion Batteries: Bridging the Gap from Academia to Industry for Grid-Scale Energy Storage. *Angew. Chem. Int. Ed.* **2024**, *63*, e202400045. https://doi.org/10.1002/anie.202400045.
12. Zhang, F.; Zhang, W.; Wexler, D.; et al. Recent Progress and Future Advances on Aqueous Monovalent-Ion Batteries towards Safe and High-Power Energy Storage. *Adv. Mater.* **2022**, *34*, 2107965. https://doi.org/10.1002/adma.202107965.
13. Zhang, Y.C.; Ji, X.Y.; Xie, C.D.; et al. Aqueous Secondary Batteries: Status and Challenges. *Energy Storage Mater.* **2025**, *77*, 104186. https://doi.org/10.1016/j.ensm.2025.104186.
14. Shi, H.; Fu, H.; Xue, G.; et al. Progress of vanadium-based oxides as cathode materials for aqueous zinc-ion batteries. *Coord. Chem. Rev.* **2025**, *545*, 216984. https://doi.org/10.1016/j.ccr.2025.216984.
15. Zeng, X.; Gong, Z.; Wang, C.; et al. Vanadium-Based Cathodes Modification via Defect Engineering: Strategies to Support the Leap from Lab to Commercialization of Aqueous Zinc-Ion Batteries. *Adv. Energy Mater.* **2024**, *14*, 2401704. https://doi.org/10.1002/aenm.202401704.
16. Li, G.; Sun, L.; Zhang, S.; et al. Developing Cathode Materials for Aqueous Zinc Ion Batteries: Challenges and Practical Prospects. *Adv. Funct. Mater.* **2024**, *34*, 2301291. https://doi.org/10.1002/adfm.202301291.
17. Bag, S.; Thakur, V.S.; Bhadra, A.; et al. Vacancy-Engineered Vanadium Cathode for Fast-Charging Aqueous Zinc Batteries of Ultra-Long Cycle Life. *Adv. Funct. Mater.* **2026**, *36*, e15788. https://doi.org/10.1002/adfm.202515788.
18. Liu, J.H.; Wang, Y.; Chen, X.; et al. Ammonium Vanadate-Based Cathodes for Practical Aqueous Zinc-Ion Batteries: Mechanisms, Optimization, and Challenges. *Adv. Funct. Mater.* **2026**, *36*, e17823. https://doi.org/10.1002/adfm.202517823.
19. Sinha, R.; Xie, X.; Yang, Y.; et al. Failure Mechanisms and Strategies for Vanadium Oxide-Based Cathode in Aqueous Zinc Batteries. *Adv. Energy Mater.* **2025**, *15*, 2404815. https://doi.org/10.1002/aenm.202404815.
20. Dai, Y.; Zhang, C.; Li, J.; et al. Inhibition of Vanadium Cathodes Dissolution in Aqueous Zn-Ion Batteries. *Adv. Mater.* **2024**, *36*, 2310645. https://doi.org/10.1002/adma.202310645.
21. Gan, Z.; Wang, N.; Ren, X.; et al. Suppresses Vanadium Dissolution via Superlattice Strategy for Practical Zinc-Vanadium Batteries with Ultralong Lifespan at Low Current Density. *Adv. Energy Mater.* **2026**, *16*, e06383. https://doi.org/10.1002/aenm.202506383.
22. Fan, X.; Zhang, Y.; Lai, G.; et al. Nucleation-Controlled Synthesis and a Unified Descriptor for Rational Interlayer Design of Vanadium-Oxide Cathodes toward High-Performance Zinc-Ion Batteries. *Adv. Mater.* **2026**, *38*, e73907. https://doi.org/10.1002/adma.73907.
23. Niu, H.; Liu, H.; Huang, W.H.; et al. Enhanced Working Voltage in Hydrated Vanadate Cathodes: Insights into [VO_6] Octahedral Distortion and V 3d Orbital Splitting. *Adv. Funct. Mater.* **2026**, *36*, e18785. https://doi.org/10.1002/adfm.202518785.
24. Guo, H.; Sotoudeh, M.; Rezeki, S.; et al. Regulating Solvent Co-Intercalation in Bi-Layered Vanadium Oxides for Zinc Batteries by Nanoconfinement Chemistry. *Angew. Chem. Int. Ed.* **2026**, *65*, e20990. https://doi.org/10.1002/anie.202520990.
25. Zong, Q.; Zhuang, Y.; Liu, C.; et al. Dual Effects of Metal and Organic Ions Co-Intercalation Boosting the Kinetics and Stability of Hydrated Vanadate Cathodes for Aqueous Zinc-Ion Batteries. *Adv. Energy Mater.* **2023**, *13*, 2301480. https://doi.org/10.1002/aenm.202301480.

26. Guo, K.; Song, Z.; Lv, Y.; et al. Inorganic–Organic Co-Intercalated $[Al_{0.16}(C_5H_{14}ON)_{0.12}]V_2O_5{\cdot}0.39H_2O$ Cathode for High-Performance Aqueous Zinc-Ion Batteries. *Adv. Funct. Mater.* **2025**, *35*, 2506036. https://doi.org/10.1002/adfm.202506036.
27. Chen, J.; Ou, G.; Liu, P.; et al. Pyrrolic-Nitrogen Chemistry in 1-(2-hydroxyethyl)imidazole Electrolyte Additives toward a 50,000-Cycle-Life Aqueous Zinc-Iodine Battery. *Angew. Chem. Int. Ed.* **2025**, *64*, e202414166. https://doi.org/10.1002/anie.202414166.
28. Niu, H.; Liu, H.; Yang, L.; et al. Impacts of distorted local chemical coordination on electrochemical performance in hydrated vanadium pentoxide. *Nat. Commun.* **2024**, *15*, 9421. https://doi.org/10.1038/s41467-024-53785-2.
29. Liu, H.; Yang, L.; Shen, T.; et al. Distorting Local Structures to Modulate Ligand Fields in Vanadium Oxide for High-Performance Aqueous Zinc-Ion Batteries. *ACS Nano* **2025**, *19*, 9132–9143. https://doi.org/10.1021/acsnano.4c18250.
30. Bi, W.; Wang, J.; Huang, T.; et al. Charge separation induced molecular polarization accelerates mass transfer in hydrated vanadate for zinc-ion storage. *Nano Energy* **2026**, *156*, 112202. https://doi.org/10.1016/j.nanoen.2026.112202.
31. Zhang, P.; Gong, Y.; Fan, S.; et al. Glutamic Acid Induced Proton Substitution of Sodium Vanadate Cathode Promotes High Performance in Aqueous Zinc-Ion Batteries. *Adv. Energy Mater.* **2024**, *14*, 2401493. https://doi.org/10.1002/aenm.202401493.
32. Xu, H.; Zhang, D.; Wang, W.; et al. Synergy of Multi-Covalent Bonds Enabling High-Performance Aqueous Zinc-Ion Battery Cathodes Toward Industrial-Grade Mass Loading and Broad-Temperature Adaptability. *Adv. Mater.* **2026**, *38*, e72906. https://doi.org/10.1002/adma.72906.
33. Fang, Y.; Qi, C.; Bao, W.; et al. Asymmetric orbital hybridization at the MXene–VO_{2-x}interface stabilizes oxygen vacancies for enhanced reversibility in aqueous zinc-ion batteries. *Energy Environ. Sci.* **2025**, *18*, 367–377. https://doi.org/10.1039/d4ee04466e.
34. Fan, B.; Huang, C.; Jiang, Z.; et al. Decoupling Electronic and Crystal Structure Effects to Overcome the Capacity-Stability Trade-Off for High-Performance Aqueous Zinc-Ion Batteries. *Adv. Funct. Mater.* **2026**, *36*, e22400. https://doi.org/10.1002/adfm.202522400.
35. Xu, Y.; Yang, X.; Bu, X.; et al. Igniting Grotthuss Topochemistry in Hydrated Vanadium Pentoxide for High-Performance Aqueous Zn-Ion Batteries. *Adv. Funct. Mater.* **2026**, *36*, e76502. https://doi.org/10.1002/adfm.76502.
36. Jia, X.; Liu, C.; Wang, Z.; et al. Weakly Polarized Organic Cation-Modified Hydrated Vanadium Oxides for High-Energy Efficiency Aqueous Zinc-Ion Batteries. *Nano-Micro Lett.* **2024**, *16*, 129. https://doi.org/10.1007/s40820-024-01339-y.
37. Liu, H.; Hou, X.; Fan, S.; et al. Local Electric Field Accelerates Zn^{2+} Diffusion Kinetics for Zn-V Battery. *Adv. Energy Mater.* **2024**, *14*, 2402416. https://doi.org/10.1002/aenm.202402416.
38. Zhang, D.; Cao, J.; Yang, C.; et al. Highly Stable Aqueous Zn-Ion Batteries Achieved by Suppressing the Active Component Loss in Vanadium-Based Cathode. *Adv. Energy Mater.* **2025**, *15*, 2404026. https://doi.org/10.1002/aenm.202404026.
39. Guo, D.; Fan, Y.; Yang, Q.; et al. Oxygen-Deficient Organic/Inorganic VO_x-PPy cathode composites: Enabling prolonged lifespan of aqueous zinc-ion batteries. *Chem. Eng. J.* **2025**, *507*, 160745. https://doi.org/10.1016/j.cej.2025.160745.
40. Wu, M.; Shi, C.; Yang, J.; et al. The LiV_3O_8 Superlattice Cathode with Optimized Zinc Ion Insertion Chemistry for High Mass-Loading Aqueous Zinc-Ion Batteries. *Adv. Mater.* **2024**, *36*, 2310434. https://doi.org/10.1002/adma.202310434.
41. Cui, R.; Gu, J.; Wang, N.; et al. Organic Dye Molecule Intercalated Vanadium Oxygen Hydrate Enables High-Performance Aqueous Zinc-Ion Storage. *Small* **2024**, *20*, 2307849. https://doi.org/10.1002/smll.202307849.
42. Wang, Y.; Zhao, M.; Gao, G.; et al. Polyvinylpyrrolidone-Intercalated $Mn_{0.07}VO_x$ toward High Rate and Long-Life Aqueous Zinc-Ion Batteries. *Small Methods* **2023**, *7*, 2300606. https://doi.org/10.1002/smtd.202300606.
43. Liu, H.; Hou, X.; Fang, T.; et al. Boosting zinc-ion storage in hydrated vanadium oxides via migration regulation. *Energy Storage Mater.* **2023**, *55*, 279–288. https://doi.org/10.1016/j.ensm.2022.11.035.
44. Zhang, C.; Huang, Y.; Xu, X.; et al. Bulk-to-surface co-modification of layered hydrated vanadate cathode for aqueous zinc ion batteries. *Energy Environ. Sci.* **2024**, *17*, 4090–4103. https://doi.org/10.1039/d4ee00535j.
45. Hu, X.; Gao, S.; Lin, T.; et al. Iodine-Doped Sodium Vanadate Cathode for Improved Zn Ion Diffusion Kinetics. *Adv. Mater.* **2025**, *37*, 2416714. https://doi.org/10.1002/adma.202416714.
46. Hong, H.; Zhu, J.; Wang, Y.; et al. Metal-Free Eutectic Electrolyte with Weak Hydrogen Bonds for High-Rate and Ultra-Stable Ammonium-Ion Batteries. *Adv. Mater.* **2024**, *36*, 2308210. https://doi.org/10.1002/adma.202308210.
47. Ding, X.; Zhu, Q.; Fan, Y.; et al. High-entropy V-based cathode for high-capacity and long-life aqueous zinc-ion battery. *Nano Energy* **2025**, *136*, 110701. https://doi.org/10.1016/j.nanoen.2025.110701.
48. Wan, F.; Hao, Z.; Wang, S.; et al. A Universal Compensation Strategy to Anchor Polar Organic Molecules in Bilayered Hydrated Vanadates for Promoting Aqueous Zinc-Ion Storage. *Adv. Mater.* **2021**, *33*, 2102701. https://doi.org/10.1002/adma.202102701.
49. Liu, H.; Hou, X.; Zhang, Q.; et al. Representative By-Products of Aqueous Zinc-Vanadium Batteries: Origins, Roles, Strategies, and Prospects. *Adv. Energy Mater.* **2025**, *15*, 2406171. https://doi.org/10.1002/aenm.202406171.
50. Li, M.; Liu, M.; Lu, Y.; et al. A Dual Active Site Organic–Inorganic Poly(O-Phenylenediamine)/$NH_4V_3O_8$ Composite Cathode Material for Aqueous Zinc-Ion Batteries. *Adv. Funct. Mater.* **2024**, *34*, 2312789. https://doi.org/10.1002/adfm.202312789.

51. Huang, J.; Liang, H.; Tang, Y.; et al. *In Situ* Induced Coordination between a "Desiccant" Interphase and Oxygen-Deficient Navajoite towards Highly Efficient Zinc Ion Storage. *Adv. Energy Mater.* **2022**, *12*, 2201434. https://doi.org/10.1002/aenm.202201434.
52. Kresse, G.; Hafner, J. Ab initio molecular dynamics for liquid metals. *Phys. Rev. B* **1993**, *47*, 558–561. https://doi.org/10.1103/physrevb.47.558.
53. Kresse, G.; Hafner, J. *Ab initio* molecular-dynamics simulation of the liquid-metal–amorphous-semiconductor transition in germanium. *Phys. Rev. B* **1994**, *49*, 14251–14269. https://doi.org/10.1103/physrevb.49.14251.
54. Blöchl, P.E. Projector augmented-wave method. *Phys. Rev. B* **1994**, *50*, 17953–17979. https://doi.org/10.1103/physrevb.50.17953.
55. Perdew, J.P.; Burke, K.; Ernzerhof, M. Generalized Gradient Approximation Made Simple. *Phys. Rev. Lett.* **1996**, *77*, 3865–3868. https://doi.org/10.1103/physrevlett.77.3865.
56. Grimme, S.; Antony, J.; Ehrlich, S.; et al. A consistent and accurate *ab initio* parametrization of density functional dispersion correction (DFT-D) for the 94 elements H-Pu. *J. Chem. Phys.* **2010**, *132*, 154104. https://doi.org/10.1063/1.3382344.
57. Wang, Y.; Chen, X.; Liu, J.H.; et al. Dual-functional nanoengineering *via* molecular pillaring and conductive hybridization for high-performance aqueous zinc-ion batteries. *Chem. Sci.* **2026**, *17*, 5115–5124. https://doi.org/10.1039/d5sc09804a.
58. Chen, J.; Su, L.; Zhang, X.; et al. Ethylene Glycol Intercalation Engineered Interplanar Spacing and Redox Activity of Ammonium Vanadate Nanoflowers as a High-Performance Cathode for Aqueous Zinc–Ion Batteries. *ACS Sustain. Chem. Eng.* **2023**, *11*, 12467–12476. https://doi.org/10.1021/acssuschemeng.3c03386.
59. Song, Z.; Zhao, Y.; Zhou, A.; et al. Organic Intercalation Induced Kinetic Enhancement of Vanadium Oxide Cathodes for Ultrahigh-Loading Aqueous Zinc-Ion Batteries. *Small* **2024**, *20*, 2305030. https://doi.org/10.1002/smll.202305030.